TU Delft

Delft University of Technology

Document Version
Final published version

Licence
CC BY

Citation (APA)
Tazi, M. A., Jebli, M., Wu, Y., Teixeira De Freitas, S., Casari, P., & de Barros, S. (2026). Hybrid flax/carbon bonded composite patches for strengthening of steel plates: layup and adhesive effect. *Journal of Adhesion*. https://doi.org/10.1080/00218464.2026.2714433

Important note
To cite this publication, please use the final published version (if applicable).
Please check the document version above.

Copyright
In case the licence states “Dutch Copyright Act (Article 25fa)”, this publication was made available Green Open Access via the TU Delft Institutional Repository pursuant to Dutch Copyright Act (Article 25fa, the Taverne amendment). This provision does not affect copyright ownership.
Unless copyright is transferred by contract or statute, it remains with the copyright holder.

Sharing and reuse
Other than for strictly personal use, it is not permitted to download, forward or distribute the text or part of it, without the consent of the author(s) and/or copyright holder(s), unless the work is under an open content license such as Creative Commons.

Takedown policy
Please contact us and provide details if you believe this document breaches copyrights.
We will remove access to the work immediately and investigate your claim.

This work is downloaded from Delft University of Technology.



The Journal of Adhesion

ISSN: 0021-8464 (Print) 1545-5823 (Online) Journal homepage: www.tandfonline.com/journals/gadh20

Hybrid flax/carbon bonded composite patches for strengthening of steel plates: layup and adhesive effect

Mohamed Amine Tazi , Mouad Jebli , Yuan Wu , Sofia Teixeira De Freitas, Pascal Casari & Silvio de Barros

To cite this article: Mohamed Amine Tazi , Mouad Jebli , Yuan Wu , Sofia Teixeira De Freitas, Pascal Casari & Silvio de Barros (17 Aug 2026): Hybrid flax/carbon bonded composite patches for strengthening of steel plates: layup and adhesive effect, The Journal of Adhesion, DOI: 10.1080/00218464.2026.2714433

To link to this article: https://doi.org/10.1080/00218464.2026.2714433

Published online: 17 Aug 2026.

Submit your article to this journal

Article views: 16

View related articles

View Crossmark data

Full Terms & Conditions of access and use can be found at
https://www.tandfonline.com/action/journalInformation?journalCode=gadh20

THE JOURNAL OF ADHESION
https://doi.org/10.1080/00218464.2026.2714433

Taylor & Francis
by informa

Check for updates

Hybrid flax/carbon bonded composite patches for strengthening of steel plates: layup and adhesive effect

Mohamed Amine Tazi[a], Mouad Jebli[a], Yuan Wu[b], Sofia Teixeira De Freitas[c,d], Pascal Casari[b], and Silvio de Barros[a,e]

[a]CESI, CESI LINEACT, UR 7527, Paris, France; [b]Department of Civil and Mechanical Engineering, Nantes Université, GeM, Saint-Nazaire, France; [c]IDMEC, Instituto Superior Técnico, Universidade de Lisboa, Lisboa, Portugal; [d]Department of Aerospace Engineering, TU Delft, Delft, The Netherlands; [e]CEFET/RJ, Federal Center for Technological Education of Rio de Janeiro, Rio de Janeiro, Brazil

ABSTRACT

Adhesive bonding of Fiber-Reinforced Polymer (FRP) patches is increasingly used to strengthen steel structures. Considering that carbon FRP (CFRP) and epoxy adhesives are the primary materials in industrial applications, this study explores the feasibility of hybridizing CFRPs with Flax FRPs (FFRPs) and the effects of using different adhesives on the mechanical performance of reinforced steel plates under flexural loading. Four configurations of composite layups were manufactured, namely: F5 (flax), C5 (carbon), CF3C and F3C2 (carbon/flax hybrids). These patches were bonded to steel plates using three adhesives: a rigid and brittle epoxy (adhesive A), a medium flexibility-ductility acrylate (adhesive B), and highly flexible ductile silane-modified polymer (adhesive C), representing a wide range of adhesive properties. Quasi-static three-point bending tests were conducted to evaluate mechanical performance of these novel hybrid composite-adhesive-steel structures compared to unreinforced steel plates, and Digital Image Correlation (DIC) was performed to monitor displacements and strains on the outer surface of the composite patch. Furthermore, finite element models were built and validated by experimental data, which were then used to predict development of stresses in each part of the assembly. Overall, it has been demonstrated that composite patch bonding can significantly enhance the load-bearing capacity of the reinforced steel substrate. Adhesive A provided the highest flexural strengthening but displayed brittle failure behavior, followed by adhesive B which showed second best flexural strengthening performance while keeping a ductile behavior at failure. Adhesive C showed poor flexural strengthening enhancement due to the poor stress transfer capabilities of the adhesive. Hybrid F3C2 and CF3C configurations achieved flexural performance comparable to pure carbon (C5), highlighting the potential of hybrid designs for structural applications.

ARTICLE HISTORY
Received 4 March 2026
Accepted 27 July 2026

KEYWORDS
Steel structural strengthening; hybrid carbon/flax composites; adhesively bonded repairs; three-point bending tests

1. Introduction

Composite materials have long been used in civil engineering, particularly to strengthen structural elements like bridge beams.[1] Though composite

CONTACT Mohamed Amine Tazi matazi@cesi.fr CESI, CESI LINEACT, UR 7527, Paris, France
© 2026 Taylor & Francis Group, LLC

reinforcement of concrete is well established, the use of carbon fiber-reinforced polymers (CFRPs) for metallic structures has attracted increasing attention in recent years, due to their applicability in limited-access zones and when fast, cost-effective installation is needed.[2] Studies have shown that bonding CFRP strips to steel beams can significantly improve load-bearing capacity and post-yield stiffness.[2–5] Guidelines from CIRIA[6] and ICE[7] also support the application of CFRP in metal structure rehabilitation.

Compared to other joining methods such as riveting and bolting, adhesive bonding is a preferred technology for joining composite structures as it provides remarkable stress transfer mechanisms and design flexibility.[8] Adhesive bonding induces less critical stress concentration areas by spreading the loads on wider surfaces and does not adversely impact the mechanical properties of substrates. The effectiveness of this joining method mainly depends on several critical parameters including the substrate type, surface treatment of bonded area and loading specifications during service.[9–12] Adhesively bonded composite repair technology seems to become the favored solution for the rehabilitation of many metallic structures such as beams,[4] decks,[13] pipes,[14,15] tanks[16] and ship hulls.[17] In the repair process, the Fiber-Reinforced Polymer (FRP) patch is usually applied either to restore the initial mechanical properties of the structure by compensating for corrosion section loss or preventing crack propagation, or to strengthen the structure and thus improve the initial load-bearing capacity.

To date, the majority of structural composite reinforcements have relied on epoxy-based adhesives, which can offer excellent stiffness, high strength, and long-term durability.[18] However, many conventional structural epoxies are relatively stiff and exhibit low strain-to-failure behavior (often only a - few percent in common formulations), so they are sensitive to differential deformation between adherends. This becomes particularly problematic when bonding ductile substrates such as structural steels, which can undergo significant elastic tensile strains under Multiphysics loadings. In such cases, more ductile adhesives – such as polyurethane, acrylic, or silane-modified polymer systems – could offer advantages by accommodating greater strain and reducing the risk of sudden interfacial failure or debonding under dynamic or impact loads.[19] Although these adhesives often exhibit lower stiffness and strength than epoxies, they may enhance energy dissipation, increase joint toughness, and extend the service life of the bonded repair. The balance between adhesive ductility and strengthening efficiency has been continuously explored, especially for retrofitting steel structures in seismic or fatigue-prone environments.[20]

So far, the majority of FRP materials used for structural purposes consist of either Carbon FRP (CFRP) or Glass FRP (GFRP), typically with epoxy resins and adhesives derived from petrochemical sources.[4] However, growing environmental concerns regarding the carbon footprint, non-renewability,

and end-of-life disposal of synthetic materials have driven increasing interest in greener alternatives.[21] Among natural fibers, flax fibers stand out due to their excellent specific mechanical properties, renewability, low energy consumption during production, and favorable life-cycle assessment,[21–23] making Flax Fiber-Reinforced Polymers (FFRPs) attractive from both sustainability and manufacturing perspectives, compared to their carbon and glass counterparts. Nonetheless, FFRPs suffer from intrinsic drawbacks, such as lower tensile strength and stiffness, increased variability in fiber quality, and pronounced sensitivity to environmental conditions, especially moisture and elevated temperatures. These factors currently limit their application to semi-structural or non-structural applications, such as automotive interiors, sports equipment, or temporary building solutions.[21]

To overcome the mechanical limitations of flax composites while preserving their environmental benefits, hybridization strategies[24] have emerged, particularly combining flax and carbon fibers within the same laminate. This hybrid approach takes advantage of the mechanical synergy between the low density and good damping properties of flax fibers, and the high stiffness, strength, and moisture resistance of carbon fibers. By optimizing the stacking sequence and interfacial compatibility, flax/carbon hybrid laminates can achieve tailored mechanical responses—e.g., delayed failure onset, progressive damage development, and improved impact resistance – while partially reducing the environmental and economic cost of using pure carbon composites.[25,26] Moreover, the progressive failure behavior of flax fibers may serve as a natural warning system prior to catastrophic rupture, which is particularly beneficial in structural applications. These hybrid composites are now being investigated owing to their potential in load-bearing retrofits, especially when paired with adhesive technologies that match the mechanical and thermal properties of both the substrate and the reinforcement.

In this study, in order to evaluate the effects of adhesive type and composite patch configuration on flexural performance, four configurations of composite layups were manufactured, including F5 (flax), C5 (carbon), CF3C and F3C2 (carbon/flax hybrids), and subsequently bonded to steel plates using three types of structural adhesives, appropriate for steel-to-FRP joining: a rigid brittle adhesive (A), a medium flexibility-ductility acrylate (B), and a highly flexible ductile silane-modified polymer (C), representing a wide range of adhesive properties. Three-point bending tests were conducted to evaluate mechanical performance of these novel hybrid composite-adhesive-steel structures compared to unreinforced reference steel specimens, and Digital Image Correlation (DIC) have been used for strain monitoring on the outer surface of the composite patch. Finite Element (FE) numerical models have been developed, validated by comparison with experimental results, and finally used to predict the developed stresses on each part of the assembly. By combining experimental and numerical approaches, this study aims to

highlight the potential of hybrid flax/carbon FRPs compared to conventional CFRPs for steel strengthening, and how can the choice of adhesives enhance this potential in FRP-steel bonded joints.

2. Materials

2.1. Steel substrate

The metallic substrate used in this study is ASTM A36 steel.[27] Tensile tests were performed to characterize the steel material. Figure 1 presents the tensile engineering stress-strain test curves of four steel specimens, and Table 1 presents the obtained mechanical properties in accordance with ASTM standard E8/E8M[28] for tensile testing of metallic materials. Strains were monitored using strain gauges.

2.2. Composite substrate

A 200 g/m^2 3K carbon fiber twill weave fabric from Composite Distribution® manufacturer, and a 315 g/m^2 flax fiber twill weave fabric from Sicomin® were

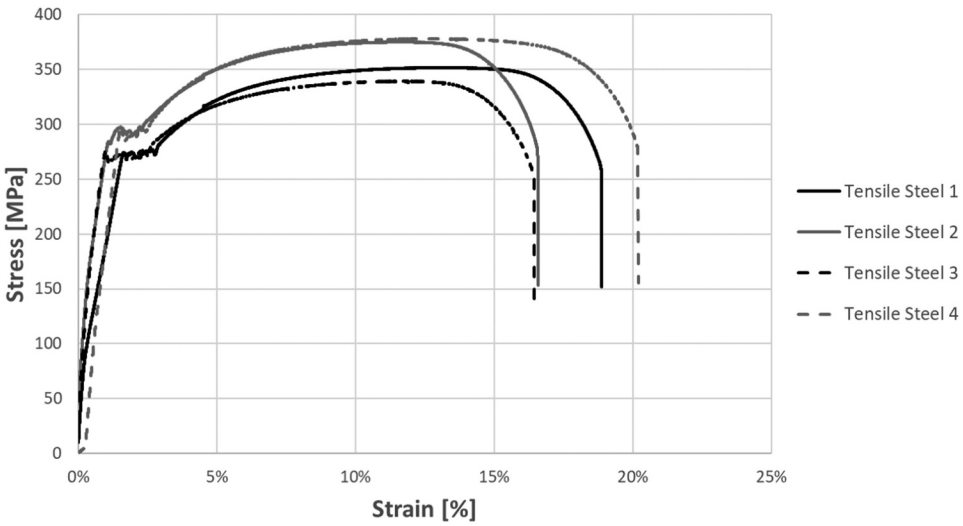


Figure 1. Engineering stress-strain curves of tensile tests on steel specimens.

Table 1. Mechanical properties of ASTM A36 steel (mean ± standard deviation).

Mechanical properties	ASTM A36 Steel
Young's modulus E	202 ± 7 GPa
Poisson ratio μ	0.27 ± 0.01
Yield strength $R_{p0,2}$	282 ± 30 MPa
Ultimate tensile strength σ_u	373 ± 7 MPa
Failure strain ε_f	18.6 ± 2.4%

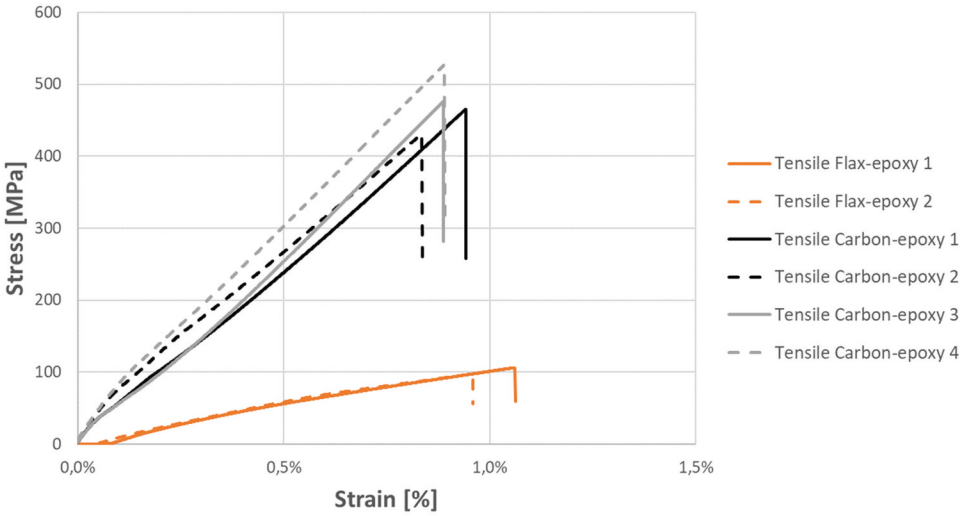


Figure 2. Engineering stress-strain curves of tensile tests on FRP specimens.

used as reinforcements for the composite material. The matrix used was a 35% bio-based epoxy resin, SR GreenPoxy 33, combined with the SD 4773 hardener, both supplied by Sicomin®. The resin and hardener were mixed at a 100:27 weight ratio. All the composite materials were manufactured using a vacuum assisted resin infusion process, in accordance with the supplier's recommendations.[29] The vacuum pump ensured a minimum absolute pressure of 100 mbar, and after infusion, the manufactured composite plates were left to cure at room temperature for 24 h before undergoing post-curing at 40°C for an additional 24 h.

Specimens of flax/epoxy composite $[0/90]_5$ and carbon/epoxy $[0/90]_5$ were manufactured and tested, and their engineering tensile stress-strain curves are presented in Figure 2. Strains were monitored using strain gauges and a clip-on extensometer for the flax/epoxy composite. Table 2 presents the mechanical properties of the composite materials used in this study, which are obtained in accordance with ASTM D3039[30] for tensile testing of polymer matrix composites. Given the rectangular geometry of the specimens and the absence of gripping tabs, failure tended to occur near the grips. As a result, the measured ultimate tensile strength and strain are likely to represent conservative estimates of the material's true performance.

Table 2. Mechanical properties of carbon/epoxy and flax/epoxy composites (mean ± standard deviation).

Mechanical properties	Carbon/epoxy	Flax/epoxy
Young's modulus $E_1 \simeq E_2$	53.4 ± 4.8 GPa	9.3 ± 0.7 GPa
Poisson ratio μ_{12}	0.12 ± 0.02	0.15 ± 0.01
Ultimate tensile strength σ_u	>475 ± 40 MPa	>102 ± 6 MPa
Failure strain ε_f	>0.89 ± 0.06%	>1.10 ± 0.02%

Table 3. Mechanical properties of sika® adhesives (based on datasheets[31–33]).

Industrial name	Nomenclature	Young's modulus [MPa]	Tensile strength [MPa]	Tensile lap-shear strength [MPa]	Tensile failure strain [%]	Critical energy release rate G_{Ic} [N/mm]
SikaPower®-1200	A	2600	40	20	3.5	3.5
SikaFast®-555 L05	B	–	11	12	200	–
SikaFlex®-554	C	–	3.5	2.5	500	–

2.3. Adhesives

Three adhesives supplied by Sika® France, specifically selected owing to their compatibility to steel/composite bonding, were studied in this work:

- SikaPower®-1200: Rigid and brittle Epoxy adhesive (Adhesive **A**).
- SikaFast®-555 L05: Medium flexibility and ductility Acrylate adhesive (Adhesive **B**).
- SikaFlex®-554: Flexible and ductile Silane Modified Polymer (Adhesive **C**).

As shown in Table 3, these structural adhesives can cover a wide range of mechanical behaviors, from highly flexible and ductile to rigid brittle. This makes it possible to assess the influence of adhesive type on the induced strengthening behavior. Table 3 summarizes the chosen nomenclatures to designate each adhesive, and presents their relevant mechanical properties based on manufacturer datasheets.[31–33]

3. Specimen manufacturing process

The manufacturing process of the steel/composite bonded specimens required three main stages, namely: manufacturing of composite patch configurations, surface preparation of adherends and the final bonding. These operations are detailed in what follows.

Figure 3 represents the nominal dimensions and geometry of the specimens. The thickness of the steel plate was measured at three points (at the middle and at the two edges) for seven specimens, and was indeed found to be 4.0 ± 0.1 mm.

3.1. Composite patch configurations

Table 4 lists the four patch configurations manufactured. All bidirectional plies are oriented at [0/90] regardless of configuration. Particular attention should be given to configuration F3C2, since it is the only asymmetric

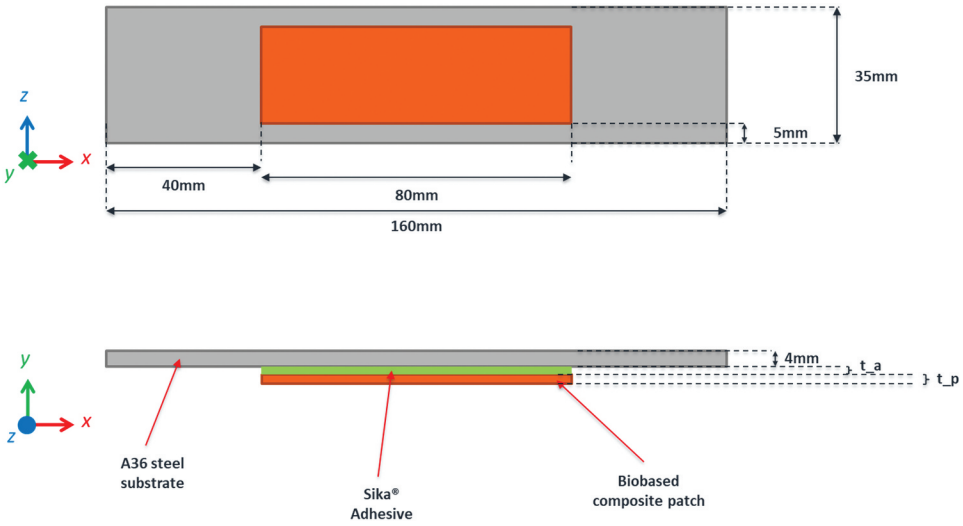


Figure 3. Specimen geometry and dimensions. t_a: thickness of the adhesive, and t_p: thickness of the composite patch.

Table 4. Manufactured composite patch layup configurations.

Configuration name	Representation	Nominal thickness [mm]	Measured thickness (mean ± standard deviation) [mm]	Number of CFRP plies	Number of FFRP plies
C5		2	1.88 ± 0.21	5	0
F5		3.5	3.46 ± 0.07	0	5
CF3C		2.9	2.72 ± 0.03	2	3
F3C2		2.9	2.78 ± 0.04	2	3

configuration, the flax fibers are the ones in contact with the adhesive, i.e. closest to the steel adherend.

3.2. Surface preparation

Surface preparation is the key step before the final structural bonding. It should not be neglected, as poor interfacial adhesion can drastically reduce the mechanical properties of the assembly.[34] This section describes the thorough surface preparation process of both used adherends.

3.2.1. Steel adherend

The surface preparation was carried out carefully following three steps:

(1) Initial cleaning with isopropyl alcohol, to remove coarse rust stains and contaminants.
(2) Manual sandblasting using SEMANAZ® RUGOS 2000–50/80 abrasive. The blasting pressure was maintained within the range of 5.5–7 bar, and the nozzle-to-surface distance was approximately 20 cm. To ensure consistency, the procedure was always carried out by the same operator.
(3) Second cleaning with isopropyl alcohol to remove any traces of grease or residue, to ensure a clean surface ready for adhesive application.

The steel substrates were subsequently stored in a vacuum desiccator containing silica gel to maintain a moisture-free environment, and the bonding process was performed within 24h.

Figure 4 shows the visual difference between the steel substrate before and after surface preparation. The surface with higher quality is referred to as "white metal" surface.

The quality of the surface treatment was assessed by roughness analysis using the Keyence® VHX-7000 Series numerical microscope. Roughness measurements were carried out in accordance with the ISO 21920–2:2021 standard on Geometrical Product Specification (GPS) – Surface texture: Profile.[35] Table 5 displays the chosen microscope parameters configured before performing roughness measurements. Table 6 presents the results of roughness analysis on seven steel samples.

3.2.2. Composite adherend

Surface preparation of the composite patches involved manual abrasion with Struers® FEPA P#180 sandpaper. The specimens were subsequently cleaned with isopropyl alcohol to remove any surface dust, then left in a fume hood for at least 15 minutes to allow the complete evaporation of isopropyl alcohol prior to bonding.

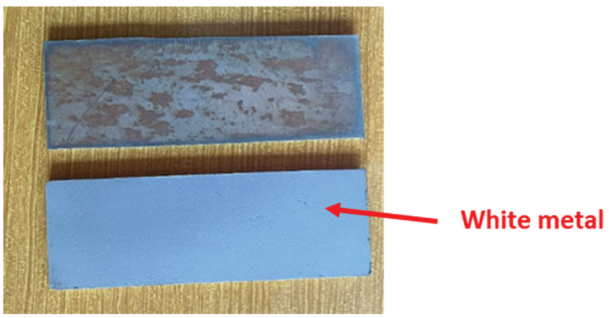


Figure 4. Steel substrate before (on top) and after (the white below) surface preparation.

Table 5. Microscope parameter setting for on-line roughness analysis in accordance with ISO 21920–2:2021.

Microscope parameters	Magnification	λ_s Filter	λ_c Filter	Evaluation length $l_n = 5 \times \lambda_c$
Values	x500	8 µm	2.5 mm	12.5 mm

Table 6. Roughness analysis results.

	Arithmetic average roughness R_a [µm]	Maximum height of the profile R_z [µm]
Target value[36]	1.5–2.5	–
Obtained value (mean ± standard deviation)	1.52 ± 0.50	12.35 ± 5.87

3.3. Bonding process

To develop a high-performance joining structure, controlling the bonding area and the thickness of the adhesive joint is the key procedure when bonding the composite patches to the steel substrates. Control of the bonding area was carried out using two 3D printed molds. Firstly, a 3D printed mold was positioned at the top of the metal to limit the spreading of the adhesive outside the patch area, as shown in Figure 5(a), allowing excess adhesive to be removed. Secondly, the adhesive was applied using a glue gun in the form of a triangular bead, as shown in Figure 5(b). The composite patch was then deposited on top of the adhesive (see Figure 5(c)) and pressed using 3D-printed U-shaped bracket designed to achieve repeatability over the thickness of the joint and ensure its parallelism relatively to the steel surface (see

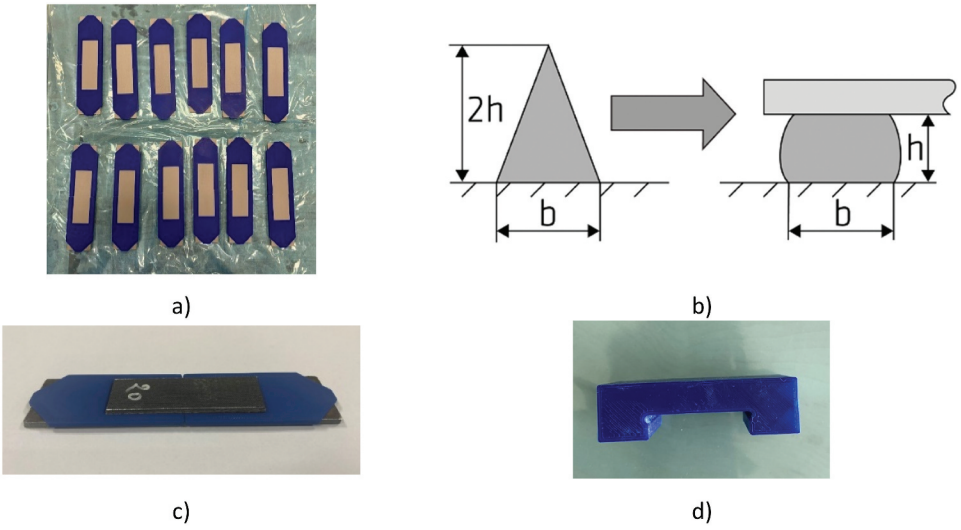


Figure 5. a) Bonding area control using a 3D-printed part, b) Target triangular bead shape of adhesive joint, c) Housing of the composite patch in the bonding area and d) 3D-printed U-shaped bracket.

Table 7. Nomenclature of the test specimens and adhesives thicknesses.

Patch layup Adhesive	F5	C5	F3C2	CF3C	t_adhesive [mm] (ave +/-STD)
Type A	A/F5	A/C5	A/F3C2	A/CF3C	1.95 ± 0.26
Type B	B/F5	B/C5	B/F3C2	B/CF3C	1.90 ± 0.39
Type C	C/F5	C/C5	C/F3C2	C/CF3C	2.07 ± 0.51

Figure 5(d)). Adhesive joint thickness control was achieved in accordance with the application methods detailed in the technical data sheets of adhesives[31–33].

After manufacturing, the specimens were allowed to be cured at room temperature for at least 2 weeks before testing.

A geometric check of the manufactured specimens was carried out using the FARO® G08-02 mechanical arm to measure the thickness of the adhesive joints, and the results are presented in Table 7. Parallelism measurements between the top planes of composite patches and steel substrates revealed a maximum defect angle equal to 3°19'. This negligible defect in addition to the repeatable joint thickness of around 2 mm indicates the high manufacturing quality of all specimens.

4. Experimental methods

The Zwick Z050 universal test machine with a 50kN load cell was used to perform three-point bending tests on the specimens. The procedures used for the three-point bending tests were based on ASTM A370 (Standard Test Methods and Definitions for Mechanical Testing of Steel Products) and ASTM D7264 (Standard Test Method for Flexural Properties of Polymer Matrix Composite Materials)[37]. The support span was 130 mm, and the radius of both the supports and loading nose was 15 mm. Four progressive quasi-static loading-unloading cycles were performed to obtain supplementary information on residual plastic deformation of the specimens. It should however be understood that the envelopes of obtained load-deflection curves are representative of the monotonic testing of the specimens. In accordance with the standards, the loading and unloading crosshead movement rates were chosen to be 5 and 10 mm/min, respectively.

Figure 6 shows the conceived experimental set-up allowing performance of Digital Image Correlation (DIC) monitoring, together with a graphical representation of loading-unloading cycles imposed.

It can be demonstrated that bonding the composite patch to the steel substrate can enhance its mechanical performance under bending loading by quantifying quantities such as ultimate flexural load and flexural rigidity.

The ultimate flexural load refers to the maximum force recorded during the tests. The ultimate flexural load gain is calculated following Equation 1:

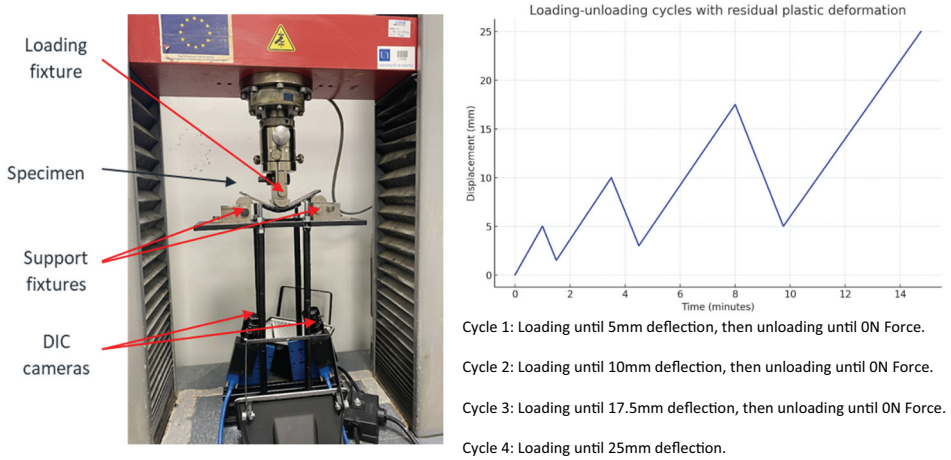


Figure 6. Three-point bending test set-up and imposed loading-unloading cycles.

$$Ultimate\ load\ gain\ (\%) = \left(\frac{F_u}{F_{u,steel}} - 1\right) \times 100 \tag{1}$$

Where F_u is the ultimate flexural load of a specimen, and $F_{u,steel}$ is the ultimate flexural load of the steel reference specimen.

The flexural rigidity was calculated by linear regression of the force values in the elastic zone during the test. Similarly, the flexural rigidity gain was calculated following Equation 2:

$$Rigidity\ gain\ (\%) = \left(\frac{k}{k_{steel}} - 1\right) \times 100 \tag{2}$$

Where k is the flexural rigidity of a specimen, and k_{steel} is the flexural rigidity of the steel reference specimen.

3D/stereo DIC was performed to monitor displacements on the outer surface of the composite patch using two 5-megapixel cameras with a 12 mm focal length from Correlated Solutions®. Calibration images and speckle images were captured using VIC-Snap software; in particular, speckle images were acquired at a frequency of 1 Hz. VIC-3D software was used for calibration and subsequent post-processing of the captured images. The stereo-DIC system was calibrated using a target-based calibration procedure with a rigid planar calibration target. The correlation options governing the accuracy of the displacement results consisted of Gaussian subset weights, optimized 8-tap interpolation, and a normalized squared differences criterion. Finally, a Lagrange tensor formulation was used for strain computation. Figure 7 shows a representation of the area of interest (AOI), and data extraction line which is positioned along the 80 mm length of the composite patch at mid-width.

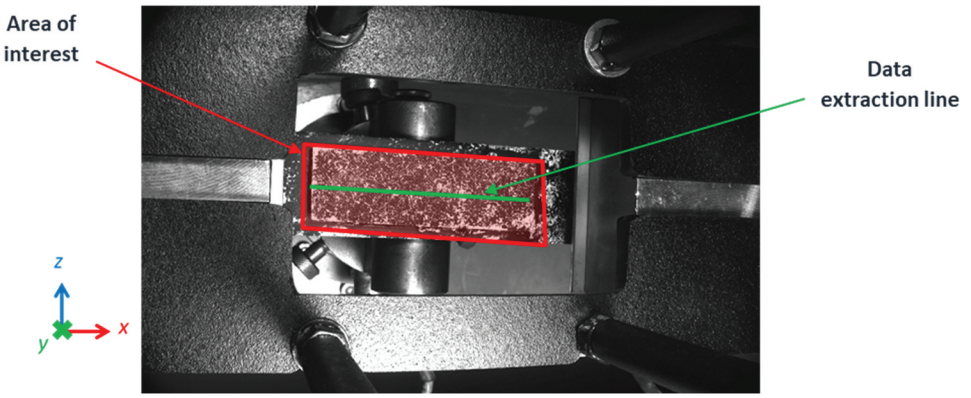


Figure 7. Area of interest (AOI) and data extraction line, at the outer surface of the composite patch via DIC monitoring.

5. Experimental results and discussion

Figure 8 shows representative Load-Deflection curves obtained during the three-point bending tests, highlighting the influence of each adhesive type, and each of the four composite patch layup configurations. Table 8 summarizes the calculated values of flexural rigidity and ultimate load gains in

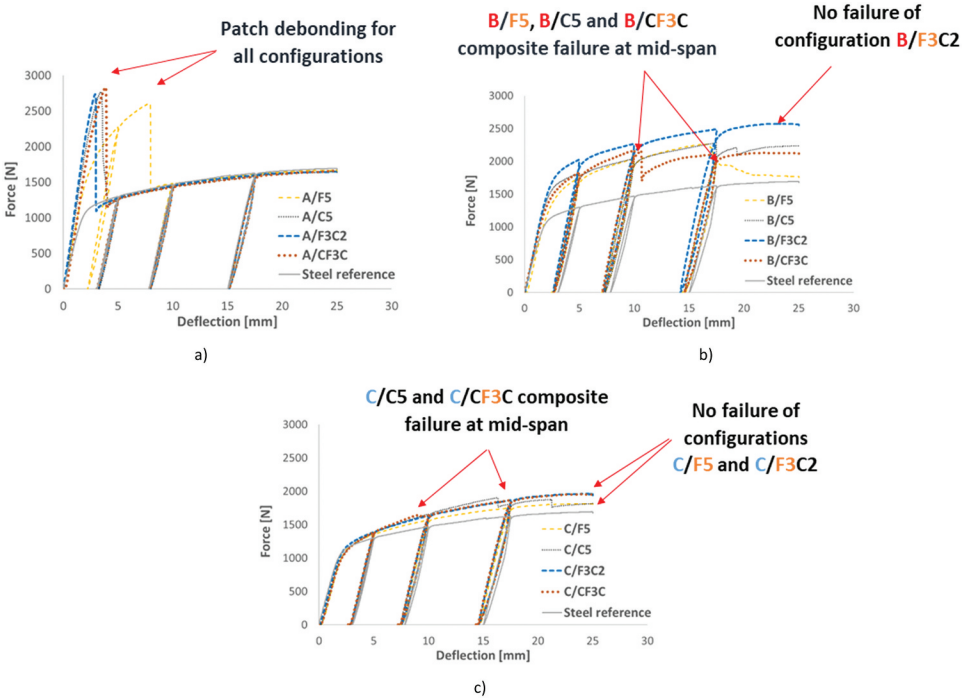


Figure 8. Load-deflection curves under three-point bending, regrouped by a) adhesive A, b) adhesive B and c) adhesive C.

Table 8. Mechanical property gains for bonded assemblies.

	Flexural rigidity (mean ± SD) [N/mm]	Flexural rigidity gain [%]	Ultimate flexural load (mean ± SD) [N]	Ultimate flexural load gain [%]	Crosshead displacement at failure [mm]	Mode of failure
Steel (Reference)	609.5 ± 7.1	–	1724.6 ± 29.0	–	–	–
A/F5	798.4 ± 40.2	31.00	2725.2 ± 109.8	58.02	8.2 ± 0.7	Patch debonding
A/C5	1032.0 ± 50.9	69.33	2833.8 ± 55.8	64.32	3.5 ± 0.1	Patch debonding
A/F3C2	1035.6 ± 14.8	69.92	2736.0 ± 18.1	58.65	3.5 ± 0.1	Patch debonding
A/CF3C	987.2 ± 35.9	61.97	2978.7 ± 134.0	72.72	3.9 ± 0.1	Patch debonding
B/F5	715.1 ± 19.5	17.33	2279.6 ± 32.1	32.18	20.6 ± 4.0	Patch failure at-midspan
B/C5	757.3 ± 15.2	24.25	2272.9 ± 42.3	31.79	19.2 ± 0.5	Patch failure at-midspan
B/F3C2	779.8 ± 38.4	27.95	2495.9 ± 67.7	44.72	–	No failure
B/CF3C	729.9 ± 19.3	19.76	2256.2 ± 77.9	30.83	11.5 ± 0.8	Patch failure at-midspan
C/F5	620.4 ± 9.3	1.79	1807.5 ± 9.5	4.81	–	No failure
C/C5	613.4 ± 10.5	0.64	1935.9 ± 56.6	12.26	21.2 ± 3.4	Patch failure at mid-span
C/F3C2	628.1 ± 5.9	3.05	1952.9 ± 52.3	13.24	–	No failure
C/CF3C	620.1 ± 7.9	1.73	1953.8 ± 0.7	13.29	9.7 ± 0.7	Patch failure at mid-span

accordance with Equation 1 and (Equation 2), the values of crosshead displacement at failure moment, and failure modes, for each steel-adhesive-patch configuration. A highly satisfying repeatability of results was observed over three tested samples per specimen type. Finally, to better identify the failure modes, Figures 9 and 10 display images of the two primary failure modes observed: patch debonding and composite patch failure. As observed in Figure 9, composite failure occurs at mid-span, while patch debonding (see Figure 10) starts at one of the edges of the joint and brutally propagates until arriving at the mid-span location. When patch debonding occurs, a thin cohesive failure can be found on the fracture surface at the steel/adhesive interface, as shown in Figure 10(b).

The configurations with adhesive A (rigid and brittle) yield the highest increase in load-bearing capacity (between +58% and +73%) in comparison with the reference steel. All specimen configurations showed a marked linear behavior prior to a sudden load drop (attributed to patch debonding, cf. Figure 10(a)), except configuration A/F5 (cf. Figure 8(a)), for which a non-linear behavior was observed at the initial stage of loading. This specific mechanical behavior could be the result of the combination of the lower elastic modulus of FFRP in comparison with CFRP, their greater strain to failure, and the intrinsic ductility of steel. The observed differences in behaviors validate the effective load transfer between the steel substrate and the composite patch. More specifically, this response suggests that the steel substrate starts plasticizing before the interfacial stresses at the steel/adhesive interface reach the critical values required to trigger debonding, partly due to the lower load-transfer efficiency of the flax composite patch. However, it should be noted

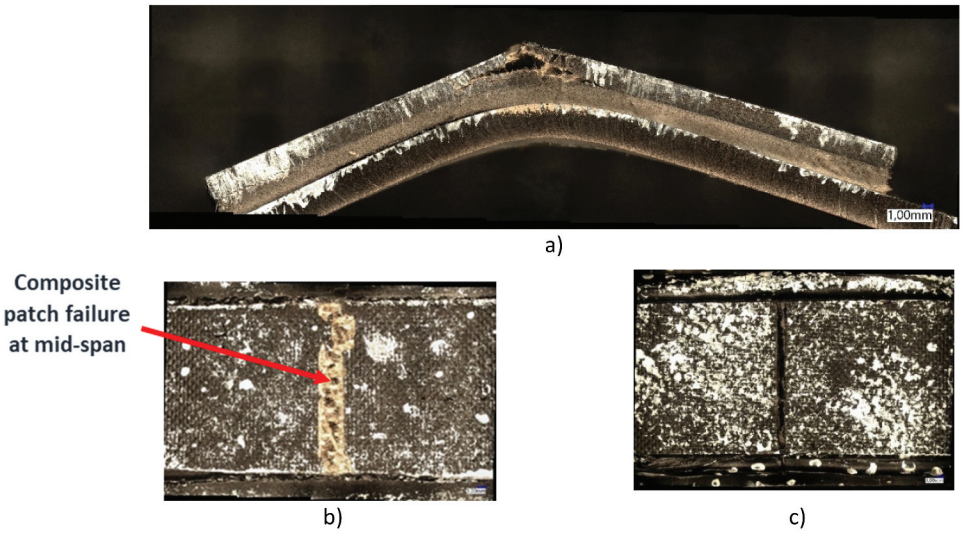


Figure 9. a) Microscope images of composite failure mode a) Side view, b) Bottom view with F5 composite configuration and c) With C5 configuration.

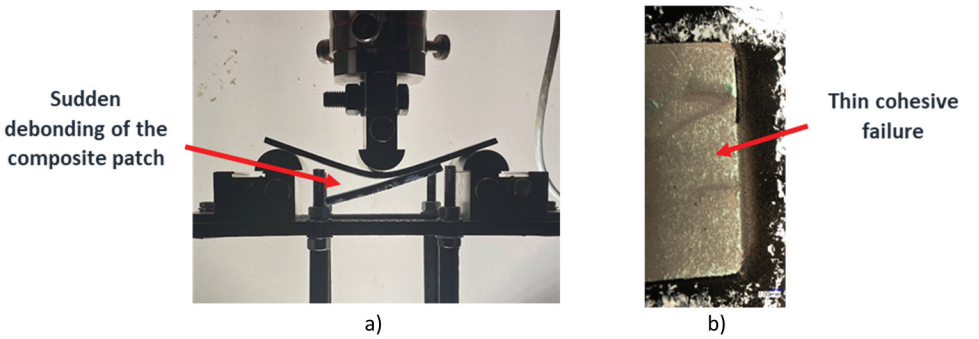


Figure 10. a) Image of patch debonding failure a) Side view and b) Thin cohesive failure.

that the rigid adhesive mainly serves the structural role and acts as the limiting factor in the assemblies, as failure occurs at the steel/adhesive interface in all cases.

In the case of joints bonded with adhesive B, a significant increase (between +32% and +45%) in the load-bearing capacity of the strengthened specimens was observed compared to the reference steel specimen. Specimens behave elastically at first, followed by nonlinear ductile behavior. It should be noted that, with this adhesive, all specimens failed due to composite patch failure at mid-span (cf. Figure 8(b)), except for the B/F3C2 configuration which did not fail at the imposed 25 mm of deflection. Furthermore, notable difference due to composite configuration is observed in the recorded loads, confirming the effective load transfer between the steel plate and the composite patch layups with this adhesive. B/F5 configuration showed the lowest level of

strengthening (+32% in ultimate load and +17% rigidity), followed by B/CF3C (+31% in ultimate load and +20% rigidity) and B/C5 (+32% in ultimate load and +24% rigidity). Finally, B/F3C2 exhibited the highest level of strengthening (+45% in ultimate load and +28% rigidity). Indeed, hybrid configurations have a greater nominal thickness than pure carbon configuration (cf. Table 4). This geometrical difference explains their comparable or higher flexural loads relative to B/C5 configuration.

Finally, with Adhesive C, a slight increase in load-bearing capacity (between +5% and +13%) was observed compared to the unstrengthened steel reference specimens, while maintaining similar ductile behavior. Only C/C5 and C/CF3C configurations failed at mid span; C/F5 and C/F3C2 configurations did not fail at the imposed 25 mm of deflection. This observation can be explained by the lower strain at failure of CFRP plies compared to FFRP ones. Moreover, small differences in strengthening performance were observed between the specimens (cf. Table 8). Since the adhesive is highly flexible and ductile, it doesn't allow proper load transfer between the steel substrate and the composite patch. This finding is backed-up by multiple interfacial stress studies,[38–40] which highlights the capabilities of flexible ductile adhesives to decrease interfacial stress concentrations at the edges of bonded joints, at the expense of stress transfer from the steel substrate to the composite patch.

Figure 11 provides a graphical representation of the mechanical property gains. It can be observed that the influence of adhesive type is usually more significant than that of the composite configuration. Some exceptions can be noted however, in particular A/F5 configuration shows a significantly lower flexural rigidity gain compared to other specimens bonded with adhesive A. Configuration B/F3C2 presents a significantly higher load and rigidity gain compared to other configurations bonded with adhesive B. Finally, configuration C/F5 shows a significantly lower load gain compared to other configurations bonded with adhesive C.

6. Finite element modeling

6.1. Model description

To replicate the performed quasi-static three-point bending test, and considering computational efficiency, 2D plane strain finite element analysis models were developed on Abaqus CAE 2024, using Abaqus Standard/Implicit solver. The aim of the models is to help better understand the development of stresses and strains in each part of the steel-adhesive-composite assembly. Figure 12 represents the geometry, boundary conditions and mesh size of the numerical model developed.

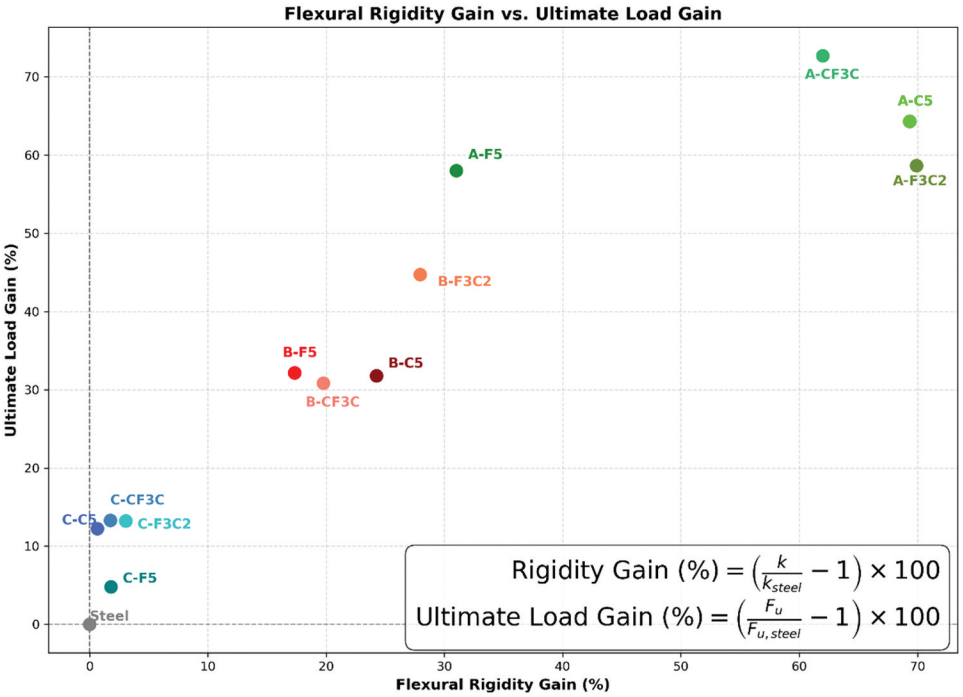


Figure 11. Graphical representation of mechanical property gains.

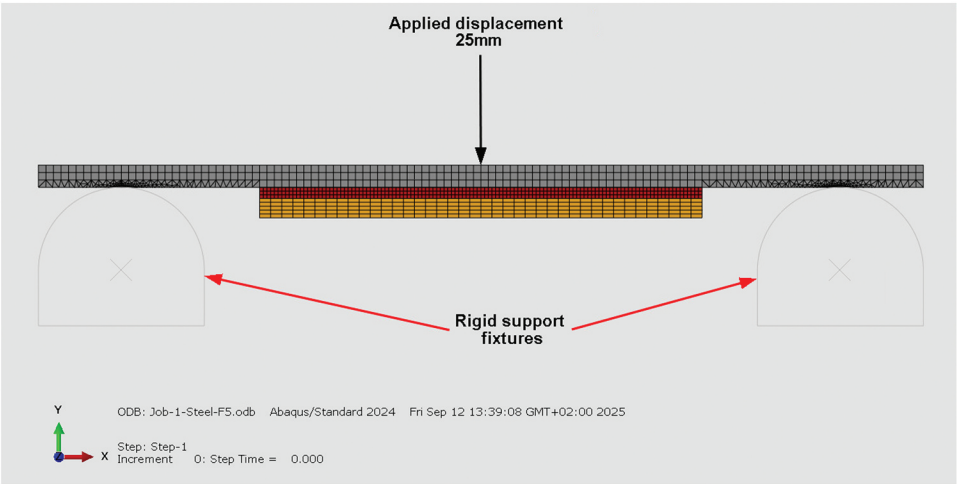


Figure 12. Visual representation of the CAE model.

Table 9 summarizes the different kinds of element types used to model each part of the assembly. Steel part is dominantly meshed with linear quadrilateral elements, and refined linear triangular elements are used in contact region with rigid supports to avoid contact numerical queries. The composite patch is meshed with quadratic quadrilateral elements, since quadratic elements have a better ability

Table 9. Element types for each part of the assembly.

Part	Element type
Steel plate	CPE4R: 4-node bilinear plane strain quadrilateral, reduced integration, hourglass control & CPE3: 3-node linear plane strain triangle
Composite patch	CPE8R: 8-node biquadratic plane strain quadrilateral, reduced integration
Adhesive A	COH2D4: 4-node two-dimensional cohesive element
Adhesive B	CPE8R: 8-node biquadratic plane strain quadrilateral, reduced integration
Adhesive C	CPE8H: 8-node biquadratic plane strain quadrilateral, hybrid, linear pressure
Fixtures	R2D2: 2-node 2D linear rigid link (for use in plane strain)

to represent curvature with a relatively coarse mesh size. Adhesive A, which fails (cf. Figure 10) is meshed with cohesive elements. Adhesive B and C, which did not fail, are meshed with quadratic quadrilateral elements. Moreover, since adhesive C is highly flexible and ductile (assumed nearly incompressible), and that it endures large strains, a hybrid formulation has been enabled to ensure convergence and better predict response of the material.[41] Naturally, a mesh convergence studies were performed to guarantee mesh-independent results. Annex A presents an example of mesh convergence study performed for B/F5 configuration model.

6.2. Material properties and modeling steps

6.2.1. Steel

The steel substrate is modeled as an isotropic material with a trilinear elastic-plastic stress-strain curve. Figure 13 presents a plot of the von mises stress-strain curve with relevant material properties.

6.2.2. Composite patch

The studied composite materials are modeled as elastic transversely isotropic linear materials. Table 10 presents the used engineering constants in the FE model.

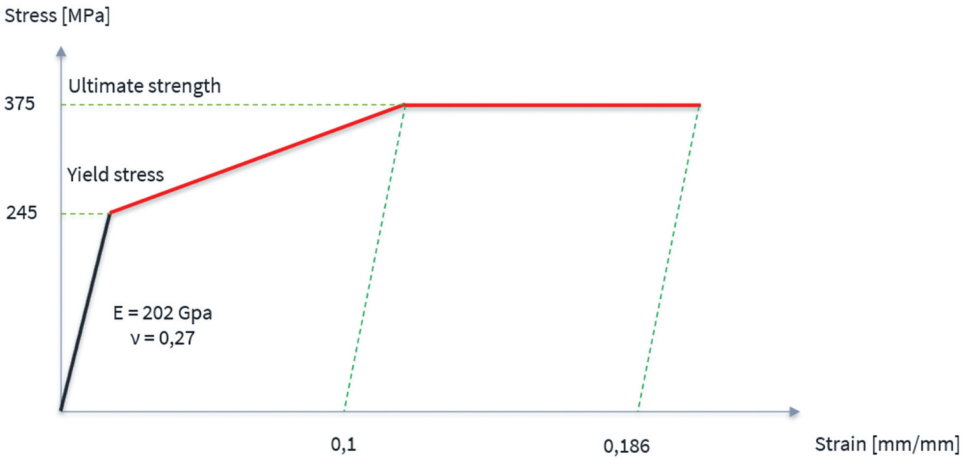


Figure 13. Modeling of material behavior of steel.

Table 10. Numerical mechanical properties of carbon/epoxy and flax/epoxy laminates.

Mechanical properties	Carbon/epoxy	Flax/epoxy
[A]Young's modulus $E_1 \simeq E_2$	53.4 GPa	9.3 GPa
[B]Young's modulus E_3	3.45 GPa	3.45 GPa
[A]Poisson ratio μ_{12}	0.12	0.15
[B]Poisson ratio $\mu_{13} \simeq \mu_{23}$	0.378	0.378
[A]Shear modulus G_{12}	23.8 GPa	4.037 GPa
[B]Shear modulus $G_{13} \simeq G_{23}$	1.2 GPa	1.2 GPa

[A]Based on experimental testing results (cf. Table 2).
[B]Out-of-plane properties were assumed to correspond to the resin mechanical properties reported in the datasheet.[29]

6.2.3. Adhesive

As mentioned above, three types of adhesives are studied and compared in this work. Considering that these adhesives exhibit different material behaviors – see Table 3, their modeling protocols differed as well. Adhesive A, which fails by debonding (cf. Figure 10), is assigned a cohesive bilinear traction-separation law due to its rigid and brittle behavior. The behavior of adhesive B, which did not fail and caused the failure of the composite patch (cf. Figure 9), has been approached by a bilinear elastic-plastic law due to its medium flexibility and ductility. Finally, the behavior of adhesive C, which did not fail and caused the failure of the patch as well, has been approached by a hyperelastic law to accommodate its high flexibility and ductility. Table 11 presents a summary of the selected modeling strategy for each type of adhesive in Abaqus and their relevant mechanical properties. In addition, the constitutive models of the adhesives are detailed in Annex. All the material properties of the adhesives are chosen in accordance with values from datasheets.[31–33]

Table 11. Numerical mechanical properties of adhesives (based on datasheets[31–33]).

Adhesive nomenclature	Modeling strategy	Mechanical properties
A	Cohesive elements Quadratic stress damage initiation criterion Energy-based evolution with linear softening, and BK law mix-mode ratio + Tie constraints	$K_{nn} = 26$ GPa/mm $K_{ss} = K_{tt} = 10$ GPa/mm $t_n^0 = 40$ MPa $t_s^0 = t_t^0 = 20$ MPa $G_n^c = 0.5$ N/mm $G_s^c = G_t^c = 1.5$ N/mm $\eta = 0.8$–1.8
B	Bilinear elastic-plastic material + Tie constraints	$E = 200$ MPa $\mu = 0.45$ $\sigma_y = 6$ MPa $\sigma_f = 11$ MPa $\varepsilon_f = 200\%$
C	Hyperelastic bulk material with Yeoh strain energy potential + Tie constraints	$C_{10} = 0.755$ $D_1 = 0.002$

6.3. Numerical modeling validation

6.3.1. Load-deflection curves

Load-deflection curves obtained in tests serve as a first basis of comparison and validation of the developed numerical model. Figure 14 shows the comparison between FEM and experimental load-deflection curves for specimens bonded to configuration F3C2. Results for the remaining configurations are presented in Annex C. Except for configuration A/F5 (cf. Annex C (b)), for which the numerical model predicts a failure at 6 mm deflection, compared to observed experimental failure around 9 mm, a good agreement between the curves can be observed. The maximum relative error on the peak load between the numerical and experimental results was 11.3%, measured for the B/CF3C configuration (cf. Annex C (d)). This comparison serves as a first validation criterion.

6.3.2. Displacements and strains

Since DIC cameras were used to monitor displacements at the outer surface of the composite patch bonded to the steel plate during three-point bending tests, comparison of DIC results with FEM results is discussed here to serve as a second basis of validation of the numerical model prior to stress analysis. Figure 15 represents a comparison of the evolution of out-of-plane displacement W (Y axis, cf. Figure 7) and first principal in-plane strain ε_{11} (X axis, fiber direction) along the 80 mm data extraction line shown in Figure 7, between DIC observations and the FEM modeling results. Results are extracted for different values of crosshead displacement d.

The numerical model accurately captures the composite patch curvature development as observed in Figure 15(a) and (e). Naturally, the highest values

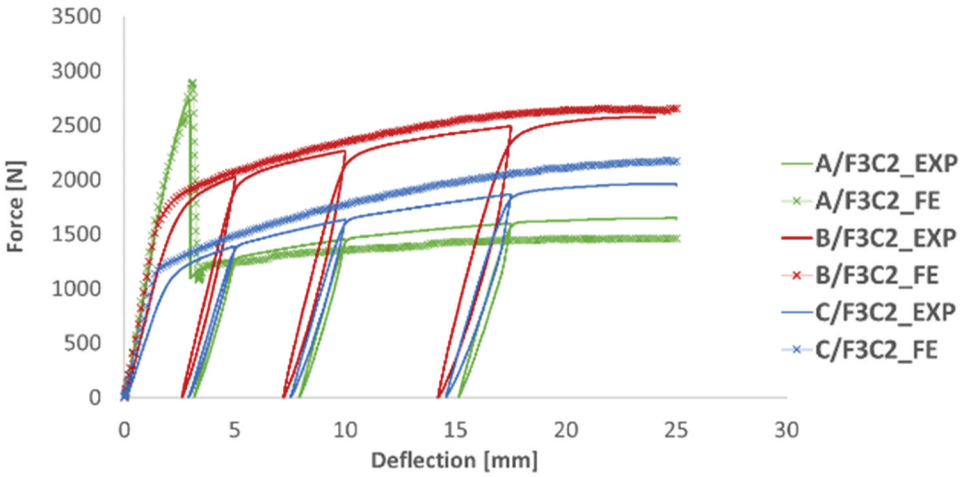


Figure 14. Comparison of experimental and FE load-deflection curves for specimens bonded with composite patch configuration F3C2.

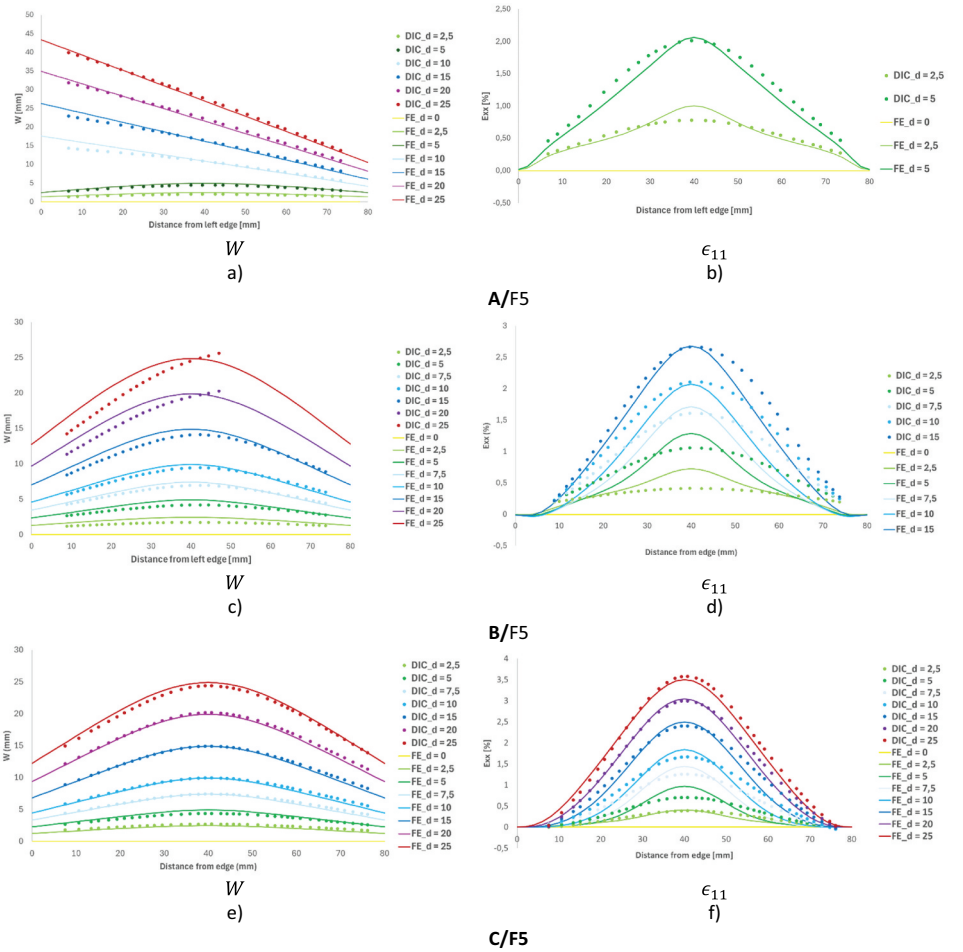


Figure 15. Comparison of DIC and FEM out-of-plane displacement W and first principal in-plane strain ε_{11} along data extraction line.

of tensile strain are in the mid-span of the composite patch as presented in Figure 15(b) and (f). It should be noted that when failure occurs (patch debonding or failure at mid-span), DIC strain information is lost, and is subsequently not presented as shown in Figure 15(b) and (d). FEM strain results are in good accordance with DIC ones, serving as a second basis of validation.

6.4. Stress analysis

To better understand the mechanisms that lead to failure in the composite patches, stress analysis is focused on the region of the patches that failed during testing. Interfacial stresses at the adhesive bondline are therefore the focus for the configurations bonded with adhesive A, as the failure was at the bondline. For the configurations bonded with adhesives B and C, the failure

occurred in the composite substrate, therefore the stress analysis is focused on the composite layers.

6.4.1. Interfacial stresses (adhesive A)

Figure 16 shows the interfacial peel t_n (Y axis, refer to Figure 12), shear t_s stresses and damage initiation criterion *QUADS* values (defined in Equation 2) along half of the bond length, starting from the composite patch edge towards mid-span. The results are extracted at 4% of the final imposed displacement, ensuring that no damage has yet been initiated in the cohesive elements. Pronounced interfacial stress concentrations are observed at the patch edges, particularly for peel stresses, which exhibit high values (up to 17.4 MPa) within the first 2 mm from the edge, then drop to almost zero stress values in the remaining bondline length (cf. Figure 16(a)). This behavior underlines the typical behavior of rigid and brittle adhesives such as adhesive A, and is consistent with analytical models of interfacial stress development in FRP-steel bonded joints.[38–40]

In terms of peel stresses in the cohesive layer, illustrated in Figure 16(a), results indicate that the highest value is obtained with A/F3C2 configuration (17.4 MPa), followed by A/C5 (15.4 MPa), A/CF3C (14.4 MPa), and finally A/F5 (10.7 MPa). Indeed, it can be discussed that the higher thickness of the flax plies induces a higher bending stiffness of the composite patch, explaining the higher peel stresses of A/F3C2 compared to A/C5.

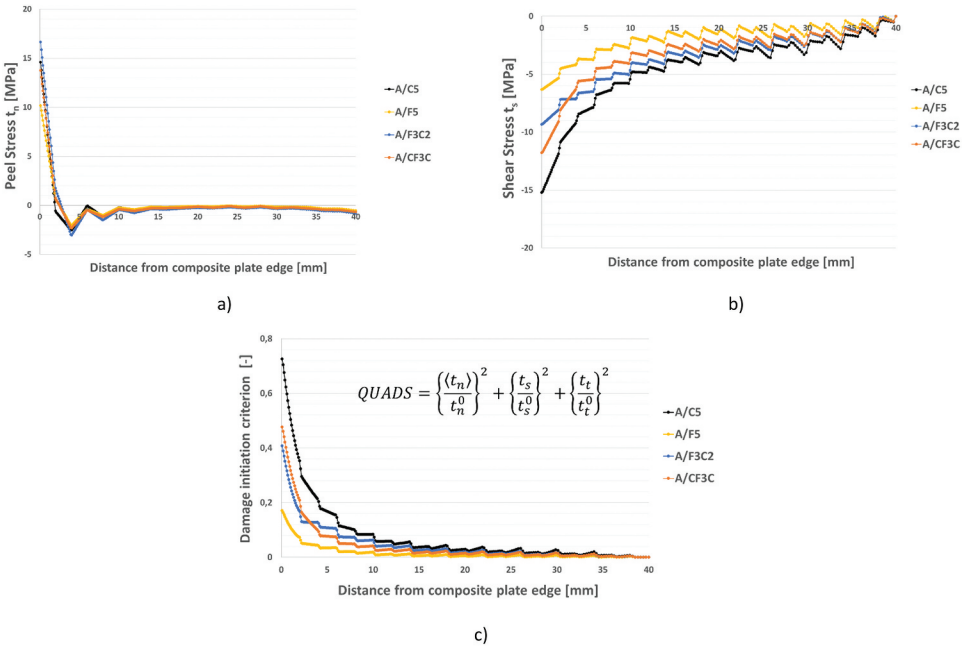


Figure 16. a) Peel b) Shear stresses, and c) Damage initiation criterion along the cohesive elements (Adhesive A) at 4% of final imposed displacement.

For shear stresses, presented in Figure 16(b), the ranking differs: cohesive layer reaches the highest peak for A/C5 configuration (15.2 MPa), followed by A/CF3C (11.8 MPa), A/F3C2 (9.3 MPa), and finally A/F5 (6.3 MPa). Indeed, shear stress development in the cohesive layer is governed by the differences of stiffness between the steel adherend and the innermost ply of the composite patch.

Finally, the value of damage initiation criterion, defined in Equation 2 is ploted in Figure 16(c). The comparison of value of criterion allows to draw conclusions on the influence of composite patch configuration on the failure initiation. It can be observed from the results that at 4% of final imposed displacement, the highest value of criterion is obtained with A/C5 configuration (0.73), followed by A/CF3C (0.48), A/F3C2 (0.41) and finally A/F5 (0.17). It can be concluded that the application of purely carbon-based patches is not always the optimal solution. As highlighted in previous studies,[42] the stiff adhesive layer is often the weak link in externally bonded composite reinforcements, and efforts on design of composite bonded patches should be performed to reduce the development of interfacial stresses in the adhesive layer. Consequently, hybrid layups, which produce lower interfacial stresses, with comparable load bearing capacity, may provide a more reliable balance between mechanical strengthening efficiency and environmental impact improvement.

6.4.2. Evolution of stresses in composite patch along thickness (adhesive B & C)

To further elucidate the role of adhesive properties on strengthening performance, the evolution of longitudinal stresses S_{11} crossing the five plies along the thickness direction of the composite patches, was analyzed at the mid-span location as shown in Figure 17. Composite plies are numbered from 1 to 5, with Ply 1 being the innermost (adjacent to the adhesive interface) and Ply 5 the outermost. The results, extracted at 5% and 50% of the respective final imposed displacement for each configuration, are presented in Figures 18 and 19.

6.4.2.1. Stress transfer at early loading stage (5% final imposed displacement).

The stress distributions at lower loading levels shown in Figure 18 reveal fundamental differences in load transfer mechanisms governed by stiffness of the adhesive.

For specimens bonded with the medium-stiffness adhesive B (Figure 18(a)), all composite plies are subjected to tensile stresses. This indicates an effective and immediate transfer of tensile strains from the bottom flange of steel substrate, through the adhesive layer, and finally into the composite patch. The sufficient rigidity of adhesive ensures that the patch acts as a true tension flange, contributing to the flexural stiffness of the assembly from the onset of loading.

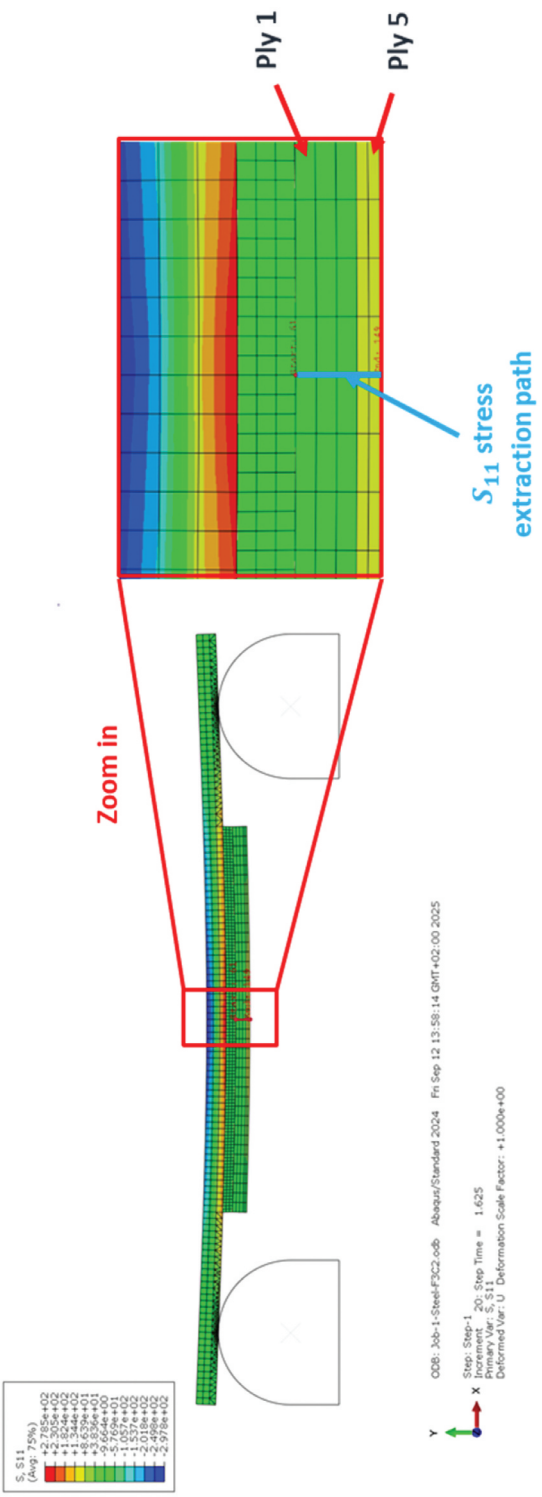


Figure 17. Visualization of data extraction path and ply numbering.

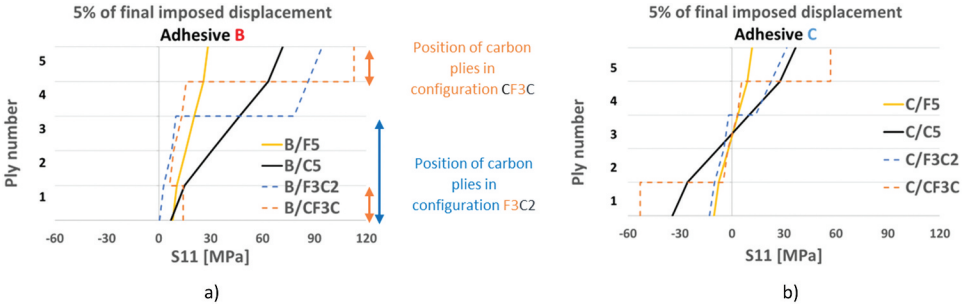


Figure 18. Longitudinal stresses S11 at 5% of final imposed displacement a) adhesive B b) adhesive C.

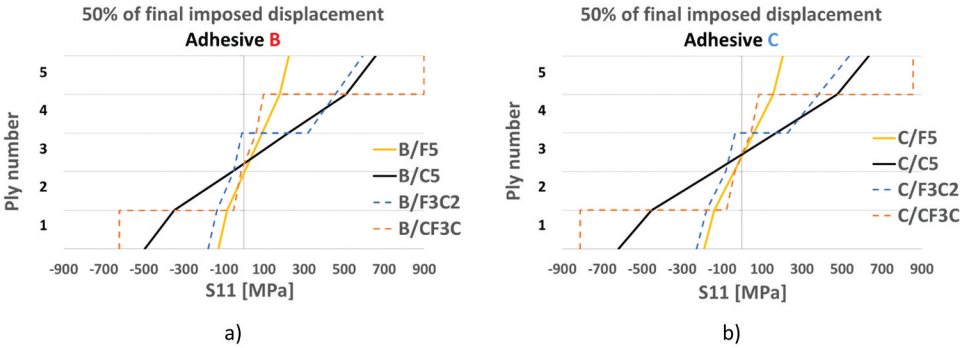


Figure 19. Longitudinal stresses S11 at 50% of final imposed displacement a) adhesive B b) adhesive C.

In contrast, for specimens bonded with the highly flexible adhesive C (Figure 18(b)), the stress state is fundamentally different. The innermost plies (1 and 2) experience compressive stresses, while the outermost plies (4 and 5) are under tension. These results are the consequence of the very low shear modulus of adhesive. Instead of being efficiently stretched by the steel substrate, the flexible adhesive layer undergoes significant shear deformation. This allows the composite patch to bend with a local curvature that is decoupled from the global curvature of the steel beam. The patch essentially behaves like a separate, lightly constrained beam resting on a soft foundation, developing its own bending moment and resulting in compression on the inner face and tension on the outer face. This mechanism severely limits the contribution of patch to the overall flexural stiffness at low loads, as validated by the minimal gains in flexural rigidity observed experimentally (Table 8).

6.4.2.2. Stress state at higher loading stage (50% final imposed displacement).

At 50% of the final imposed displacement (Figure 19), the results indicate that the composite patches exhibit a relatively similar stress state regardless of the adhesive used. However, the load-bearing capacity of the assemblies differs

significantly, as previously shown in Figure 8(b,c). This confirms that the load-transfer capability of the adhesive is a key parameter in the design of externally bonded composite patches. This could be influenced by the relatively large thickness of the adhesive layer. Hypothetically, a thinner adhesive bond line would allow for more efficient load transfer to the composite patch. Nevertheless, achieving such thin bond lines is neither straightforward nor generally recommended with this type of adhesive.

6.4.2.3. Performance of hybrid configurations. An insightful observation emerges from analyzing the stresses in the carbon fiber plies of the hybrid configurations. For B/F3C2 and C/F3C2 configurations (carbon plies positioned as Plies 4 and 5), the stress in the carbon layers at 5% load is higher than that in the outer plies of the all-carbon B/C5 and C/C5 configurations (cf. Figure 18(b,c)). This demonstrates that in the hybrid design, the stiffer carbon fibers effectively carry the load immediately, leveraging their position further from the neutral axis. As loading progresses, the stresses in the B/C5 and C/C5 configurations surpass those in the hybrids (cf. Figure 19(b,c)), indicating that the higher overall stiffness of the pure carbon patch accelerates stress development. This analysis confirms the structural efficiency of the hybrid design: the carbon fibers play their primary load-bearing role effectively, while the flax plies provide the necessary thickness to position them optimally and contribute to a more gradual stress transfer.

7. Conclusion

This study presents the manufacturing process and experimental flexural investigations of steel plates reinforced with externally bonded carbon/flax composite patches. Three adhesives were used: SikaPower®-1200 (A), SikaFast®-555 L05 (B), and SikaFlex®-554 (C), covering a range of behaviors from rigid-brittle to highly flexible-ductile. The composite materials used, consisting of carbon fibers, flax fibers and partially biobased epoxy resin, were layed-up in four patch configurations: F5 (flax), C5 (carbon), CF3C and F3C2 (carbon/flax hybrid). Three-point bending tests were performed on the specimens with DIC monitoring, and 2D plane strain FEA models were developed for stress analysis.

The existing results lead to the following conclusions:

- Bonding composite patches can significantly improve the flexural properties (up to +70% flexural rigidity gain and +73% ultimate load) of steel plates, especially with adhesives A and B.
- Regarding the effects of adhesive type and composite configurations, Adhesive A, being the most rigid, has offered the best performance in terms of flexural strengthening. The A/C5 configuration maximized flexural rigidity (+70%), while A/CF3C maximized ultimate strength (+73%).

However, brittleness of adhesive A might be problematic for certain applications where sudden failure (patch debonding) would be catastrophic.

- The compromise between flexibility and rigidity of adhesive B enables efficient load transfer, particularly with B/F3C2 configuration, with the position of the carbon plies further away from the neutral axis of the beam.
- The highly flexible behavior of adhesive C limits its effectiveness for load transfer and structural strengthening.
- For configurations bonded with adhesive A, hybridization of the composite patch leads to a decrease in the development of peel and shear stresses in the adhesive.
- In brief, hybrid carbon/flax configurations such as CF3C and F3C2 are structurally more effective and sustainable. Both of them achieved flexural responses comparable to pure carbon patches, despite the lower stiffness of flax. The B/F3C2 configuration demonstrated the most balanced performance, benefiting from strategic positioning of stiff carbon plies away from the neutral axis while leveraging flax plies for thickness, reduction of stresses in the outer plies, and environmental benefits.

In conclusion, the strengthening effectiveness of adhesively bonded composite patches is not determined solely by the stiffness of the patch and/or adhesive, but by the interaction between adhesive mechanical behavior and composite layup. Medium-modulus ductile adhesives, combined with tailored laminates that integrate carbon plies of varying stiffness with softer laminates such as flax or glass (to mitigate durability issues), emerge as a promising high-performance and sustainable solution for the flexural strengthening of steel structures.

Acknowledgments

The authors would like to express their gratitude to the GeM Institute of Research in Mechanics and Civil Engineering for providing the materials used in this study, supporting the experimental setup, and warmly welcoming them into their laboratory. We would also like to show our sincere appreciation to Sika® France for providing the adhesives, and to Sika® Engineer Mr. Jean-Pierre Jugé, for his advice and guidance in the use of the adhesives.

This work was supported by FCT, through IDMEC, under LAETA, project UIDB/50022/2020. The authors acknowledge the support of the Brazilian research agencies CNPq and FAPERJ.

Author contributions

CRediT: **Mohamed Amine Tazi:** Conceptualization, Data curation, Formal analysis, Investigation, Methodology, Software, Visualization, Writing – original draft; **Mouad Jebli:** Conceptualization, Funding acquisition, Project administration, Supervision, Validation,

Writing – review & editing; **Yuan Wu:** Investigation, Methodology, Validation, Writing – review & editing; **Pascal Casari:** Conceptualization, Formal analysis, Methodology, Project administration, Resources, Supervision, Validation; **Silvio de Barros:** Conceptualization, Funding acquisition, Project administration, Supervision, Validation.

Disclosure statement

No potential conflict of interest was reported by the author(s).

Funding

The work was supported by the Fundação Carlos Chagas Filho de Amparo à Pesquisa do Estado do Rio de Janeiro [55438bd6cdedc07932bab83e946bb872]; Fundação para a Ciência e a Tecnologia [UIDB/50022/2020].

ORCID

Mohamed Amine Tazi http://orcid.org/0009-0005-7135-2534
Silvio de Barros http://orcid.org/0000-0002-2520-569X

References

[1] Hollaway, L. *Polymer Composites for Civil and Structural Engineering*; Springer: Netherlands, Dordrecht, 1993. DOI: 10.1007/978-94-011-2136-1.
[2] Deng, J.; Lee, M. M. K. Behaviour Under Static Loading of Metallic Beams Reinforced with a Bonded CFRP Plate. *Comp. Struct.* 2007, *78*(2), 232–242. DOI: 10.1016/j.compstruct.2005.09.004.
[3] Tazi, M. A.; de Araujo Alves Lima, R.; Pires da Silva, E. H.; Jebli, M.; Teixeira De Freitas, S.; Casari, P.; de Barros, S. Experimental Evaluation of Interface Adhesion of a Flax Fiber Composite Patch with Epoxy and Polyurethane Adhesives for the Reinforcement of Steel Structures. *Int. J. Adhes. Adhes.* 2024, *129*, 103559. DOI: 10.1016/j.ijadhadh.2023.103559.
[4] Guo, D.; Wang, H.-P.; Liu, Y.-L.; Gao, W.-Y.; Dai, J.-G. Structural Behavior of CFRP-Strengthened Steel Beams at Different Service Temperatures: Experimental Study and FE Modeling. *Eng. Structu. Res.* 2023, *293*, 116646. DOI: 10.1016/j.engstruct.2023.116646.
[5] Colombi, P.; Poggi, C. An Experimental, Analytical and Numerical Study of the Static Behavior of Steel Beams Reinforced by Pultruded CFRP Strips, Composites Part B. *Compos. Eng.* 2006, *37*(1), 64–73. DOI: 10.1016/j.compositesb.2005.03.002.
[6] Stratford, T.; Cadei, J.; Hollaway, L. Ciria C595 – strengthening metallic structures using externally-bonded FRP. In *Advanced Polymer Composites for Structural Applications in Construction*, edited by Hollaway, L., Chryssanthopoulos, M. K., & Moy, S. J.; Cambridge, UK: Woodhead Publishing. 2004; pp. 693–700. DOI: 10.1533/9781845690649.7.693.
[7] Moy, S. S. J. *FRP Composites, Life Extension and Strengthening of Metallic Structures: ICE Design and Practice Guides*; Thomas Telford: London, 2001.

[8] Katnam, K. B.; Da Silva, L. F. M.; Young, T. M. Bonded Repair of Composite Aircraft Structures: A Review of Scientific Challenges and Opportunities. *Prog. Aerosp. Sci.* 2013, *61*, 26–42. DOI: 10.1016/j.paerosci.2013.03.003.

[9] Arouche, M. M.; Budhe, S.; Alves, L. A.; Teixeira de Freitas, S.; Banea, M. D.; de Barros, S. Effect of Moisture on the Adhesion of CFRP-To-Steel Bonded Joints Using Peel Tests. *J. Braz. Soc. Mech. Sci. Eng.* 2018, *40*(1), 10. DOI: 10.1007/s40430-017-0959-6.

[10] Arouche, M. M.; Budhe, S.; Banea, M. D.; Teixeira de Freitas, S.; de Barros, S. Interlaminar Adhesion Assessment of Carbon-Epoxy Laminates Under Salt Water Ageing Using Peel Tests. *Proceedings of the Institution of Mechanical Engineers, Part L: Journal of Materials: Design and Applications*, 2019; Vol. 233, pp 1555–1563. DOI: 10.1177/1464420718766626.

[11] Budhe, S.; Banea, M. D.; de Barros, S.; da Silva, L. F. M. An Updated Review of Adhesively Bonded Joints in Composite Materials. *Int. J. Adhes. Adhes.* 2017, *72*, 30–42. DOI: 10.1016/j.ijadhadh.2016.10.010.

[12] Rudawska, A. Comparison of the Adhesive joints' Strength of the Similar and Dissimilar Systems of Metal Alloy/Polymer Composite. *Appl Adhes Sci.* 2019, *7*(1), 7. DOI: 10.1186/s40563-019-0123-x.

[13] Chataigner, S.; Benzarti, K.; Foret, G.; Caron, J. F.; Gemignani, G.; Brugiolo, M.; Calderon, I.; Piñero, I.; Birtel, V.; Lehmann, F. Design and Testing of an Adhesively Bonded CFRP Strengthening System for Steel Structures. *Eng. Structu. Res.* 2018, *177*, 556–565. DOI: 10.1016/j.engstruct.2018.10.004.

[14] De Barros, S.; Banea, M. D.; Budhe, S.; De Siqueira, C. E. R.; Lobão, B. S. P.; Souza, L. F. G. Experimental Analysis of Metal-Composite Repair of Floating Offshore Units (FPSO). *J. Adhes.* 2017, *93*(1–2), 147–158. DOI: 10.1080/00218464.2016.1177514.

[15] da Costa Mattos, H. S.; Reis, J. M. L.; Paim, L. M.; da Silva, M. L.; Lopes Junior, R.; Perrut, V. A. Failure Analysis of Corroded Pipelines Reinforced with Composite Repair Systems. *Eng. Fail Anal.* 2016, *59*, 223–236. DOI: 10.1016/j.engfailanal.2015.10.007.

[16] McGeorge, D.; Echtermeyer, A. T.; Leong, K. H.; Melve, B.; Robinson, M.; Fischer, K. P. Repair of Floating Offshore Units Using Bonded Fibre Composite Materials, Composites Part a. *Compos. Appl. Sci. Manuf.* 2009, *40*(9), 1364–1380. DOI: 10.1016/j.compositesa.2009.01.015.

[17] Meniconi, L. C.; Lana, L. D.; Morikawa, S. R. Experimental Fatigue and Aging Evaluation of the Composite Patch Repair of a Metallic Ship Hull. *Appl Adhes Sci.* 2014, *2*(1), 27. DOI: 10.1186/s40563-014-0027-8.

[18] Wei, Y.; Jin, X.; Luo, Q.; Li, Q.; Sun, G. Adhesively Bonded Joints – a Review on Design, Manufacturing, Experiments, Modeling and Challenges, Composites Part B. *Compos. Eng.* 2024, *276*, 111225. DOI: 10.1016/j.compositesb.2024.111225.

[19] Galvez, P.; Abenojar, J.; Martinez, M. A. Durability of Steel-CFRP Structural Adhesive Joints with Polyurethane Adhesives, Composites Part B. *Compos. Eng.* 2019, *165*, 1–9. DOI: 10.1016/j.compositesb.2018.11.097.

[20] Delzendeh Moghadam, M.; Fathi, A.; Chaallal, O. Retrofitting of Steel Structures with CFRP: Literature Review and Research Needs. *Lit. Rev. Res. Needs Appl. Sci.* 2024, *14*(13), 5958. DOI: 10.3390/app14135958.

[21] Banea, M. D. Natural Fibre Composites and Their Mechanical Behaviour. *Polymers* 2023, *15*(5), 1185. DOI: 10.3390/polym15051185.

[22] Vigneshwaran, S.; Sundarakannan, R.; John, K. M.; Joel Johnson, R. D.; Prasath, K. A.; Ajith, S.; Arumugaprabu, V.; Uthayakumar, M. Recent Advancement in the Natural Fiber Polymer Composites: A Comprehensive Review. *J. Cleaner Prod.* 2020, *277*, 124109. DOI: 10.1016/j.jclepro.2020.124109.

[23] Shelly, D.; Singhal, V.; Jaidka, S.; Banea, M. D.; Lee, S.; Park, S. Mechanical Performance of Bio-Based Fiber Reinforced Polymer Composites: A Review. *Polym. Compos.* 2025, *46* (S3), c.30000. DOI: 10.1002/pc.30000.
[24] Masud, M.; Mubashar, A. Effect of Hybridization on the Mechanical Performance and Cost Efficiency of Carbon/Flax Bio-Hybrid Composites. *Polym. Compos.* 2024, *45*(11), 9766–9784. DOI: 10.1002/pc.28437.
[25] Wang, A.; Liu, X.; Yue, Q.; Xian, G. Hydrothermal Durability of Unidirectional Flax/Carbon Fiber Hybrid Composite Plates. *J. Mater. Res. Technol.* 2023, *22*, 2043–2061. DOI: 10.1016/j.jmrt.2022.12.021.
[26] Wang, A.; Liu, X.; Yue, Q.; Xian, G. Tensile Properties Hybrid Effect of Unidirectional Flax/Carbon Fiber Hybrid Reinforced Polymer Composites. *J. Mater. Res. Technol.* 2023, *24*, 1373–1389. DOI: 10.1016/j.jmrt.2023.03.078.
[27] A01 Committee. Standard Specification for Carbon Structural Steel. West Conshohocken, PA, USA: ASTM International. 2019, ASTM A36. DOI: 10.1520/A0036A0036M-19.
[28] E28 Committee. Standard Test Methods for Tension Testing of Metallic Materials. West Conshohocken, PA, USA: ASTM International. 2024, ASTM E8/E8M. DOI: 10.1520/E0008_E0008M-22.
[29] Sicomin®, srGreenPoxy33_sd477x. 2023. https://sicomin.com/fiches-techniques/srGreenPoxy33_sd477x.pdf.
[30] D30 Committee. Standard Test Method for Tensile Properties of Polymer Matrix Composite Materials. West Conshohocken, PA, USA: ASTM International. 2014, ASTM D3039. DOI: 10.1520/D3039_D3039M-08.
[31] Sika®, sikaflex-554. 2023. https://fra.sika.com/dam/dms/fr01/k/sikaflex-554.pdf.
[32] Sika®, sikafast-555-l05. 2023. https://che.sika.com/dam/dms/ch01/y/sikafast-555-l05.pdf.
[33] Sika®, sikapower-1200. 2023. https://industry.sika.com/dam/dms/ca01/i/sikapower-1200.pdf.
[34] Badami, A.; Raffa, M. L.; Klinkova, O.; Rizzoni, R.; Da Silva Botelho, T.; Zambelis, G. Surface Roughness Influence on the Behaviour of Biocomposite Adhesive Joints. *Int. J. Mech. Sci.* 2024, *283*, 109624. DOI: 10.1016/j.ijmecsci.2024.109624.
[35] International Organization for Standardization (ISO). Plastics — Determination of tensile properties — Part 5: Test conditions for unidirectional fibre-reinforced plastic composites. ISO 527–5:2021. https://www.iso.org/fr/standard/72226.html.
[36] Ghumatkar, A.; Budhe, S.; Sekhar, R.; Banea, M. D.; Barros, S. D. Influence of Adherend Surface Roughness on the Adhesive Bond Strength, Lat. *Lat. Am. j. Solids. Struct.* 2016, *13*(13), 2356–2370. DOI: 10.1590/1679-78253066.
[37] D30 Committee. Standard Test Method for Flexural Properties of Polymer Matrix Composite Materials. West Conshohocken, PA, USA: ASTM International. 2015, ASTM D7264. DOI: 10.1520/D7264_D7264M-21.
[38] Stratford, T.; Cadei, J. Elastic Analysis of Adhesion Stresses for the Design of a Strengthening Plate Bonded to a Beam. *Construct. Build. Mater.* 2006, *20*(1–2), 34–45. DOI: 10.1016/j.conbuildmat.2005.06.041.
[39] Deng, J.; Lee, M. M. K.; Moy, S. S. J. Stress Analysis of Steel Beams Reinforced with a Bonded CFRP Plate. *Comp. Struct.* 2004, *65*(2), 205–215. DOI: 10.1016/j.compstruct.2003.10.017.
[40] Smith, S. T.; Teng, J. G. Interfacial Stresses in Plated Beams. *Eng. Structu. Res.* 2001, *23* (7), 857–871. DOI: 10.1016/S0141-0296(00)00090-0.
[41] SIMULIA User Assistance, Hybrid incompressible solid element formulation - Assistance utilisateur SIMULIA 2025. 2025. https://help.3ds.com/2025/english/dssimu

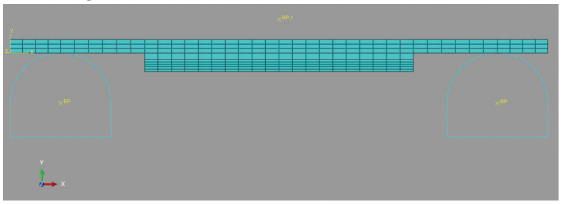
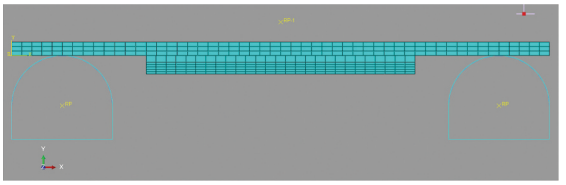
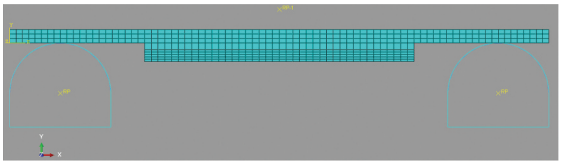
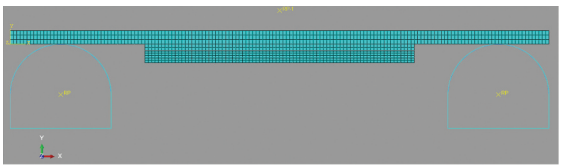
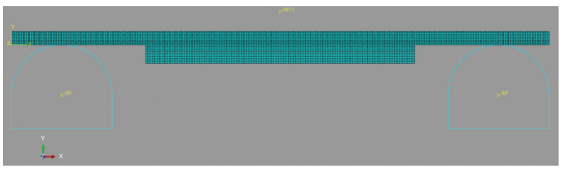
lia_established/simacaetherefmap/simathe-c-hybridincompress.htm?contextscope=all. (accessed Nov 27, 2025).

[42] Wei, K.; Chen, Y.; Li, M.; Yang, X. Strength and Failure Mechanism of Composite-Steel Adhesive Bond Single Lap Joints. *Adv Mater Sci Eng.* 2018, *2018*(1), 5810180. DOI: 10.1155/2018/5810180.

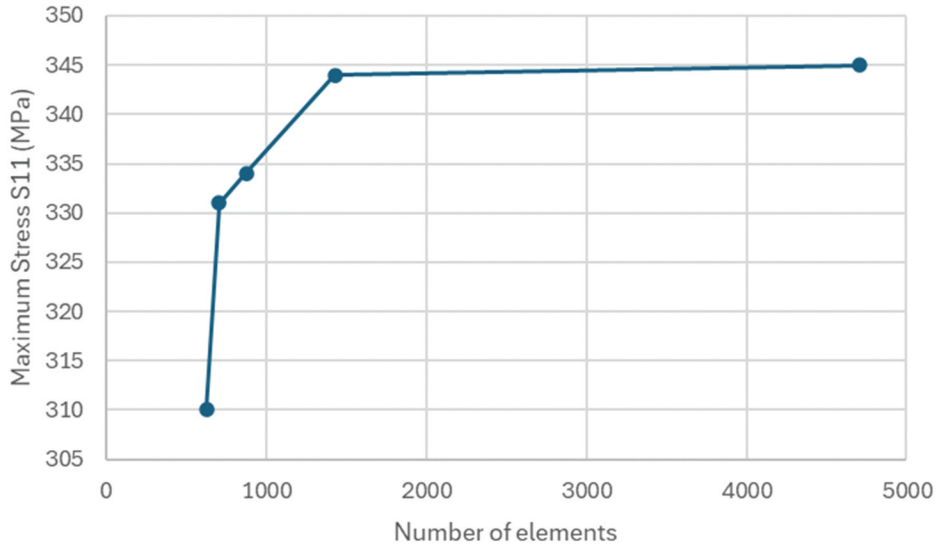
[43] Benzeggagh, M. L.; Kenane, M. Measurement of Mixed-Mode Delamination Fracture Toughness of Unidirectional Glass/Epoxy Composites with Mixed-Mode Bending Apparatus. *Compos. Sci. Technol.* 1996, *56*(4), 439–449. DOI: 10.1016/0266-3538(96)00005-X.

Annexes

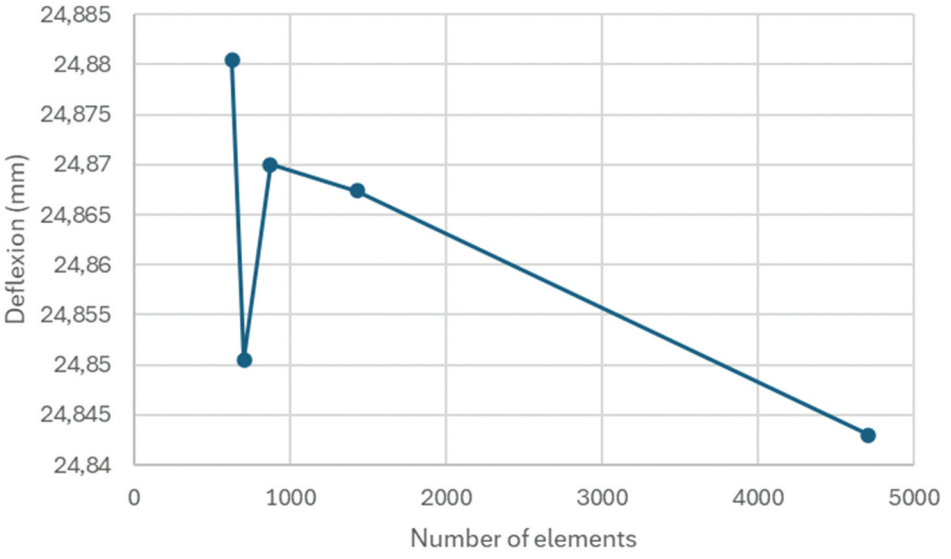
Annex A
Mesh convergence study for B/F5 configuration

Number of elements in the model	Mesh image
628	
706	
874	
1428	
4708	

The values of stress S11 and deflection w at the outer surface and mid-span of the composite patch were extracted at a displacement of 25 mm for the five models corresponding to the five mesh sizes, to perform a mesh convergence study. The results are presented below.



a)



b)

Mesh convergence study based on a) maximum stress value S11 and b) deflection at mid-span of the composite patch.

Annex B

Constitutive models of adhesives

a) Adhesive A

Adhesive A is modeled with cohesive elements following a triangular linear traction-separation law. The elastic behavior can be written as

$$\boldsymbol{t} = \begin{Bmatrix} t_n \\ t_s \\ t_t \end{Bmatrix} = \begin{bmatrix} K_{nn} & 0 & 0 \\ 0 & K_{ss} & 0 \\ 0 & 0 & K_{tt} \end{bmatrix} \begin{Bmatrix} \delta_n \\ \delta_s \\ \delta_t \end{Bmatrix} \tag{3}$$

Where t_n, t_s and t_t represent the normal (mode I) and the two shear (mode II and III) tractions, respectively. The corresponding separations are denoted by δ_n, δ_s and δ_t. Similarly, K_{nn}, K_{ss} and K_{tt} are the corresponding elastic stiffnesses. **It should be noted that $K_{nn} = \frac{E}{t}$ and $K_{ss} = \frac{G}{t}$ where E is the young's modulus of the adhesive, G the shear modulus and t is the thickness of the cohesive elements.**

The damage initiation of the cohesive layer under mixed-mode loading was predicted by the quadratic stress failure criterion

$$QUADS = \left\{\frac{\langle t_n \rangle}{t_n^0}\right\}^2 + \left\{\frac{t_s}{t_s^0}\right\}^2 + \left\{\frac{t_t}{t_t^0}\right\}^2 = 1 \tag{4}$$

Where t_n^0, t_s^0 and t_t^0 represent the peak values of the nominal stress when the deformation is either purely normal to the interface or purely in the first or the second shear direction, respectively.

Damage evolution is based on the Benzeggagh-Kenane (BK) fracture criterion,[43] which is particularly useful when the critical fracture energies during deformation purely along the first and the second shear directions are the same; that is, $G_s^C = G_t^C$. It is given by:

$$G_n^C + \left(G_s^C - G_n^C\right)\left\{\frac{G_S}{G_T}\right\}^{\eta} = G^C \tag{5}$$

Where G_n^C, G_s^C and G_t^C refer to the critical fracture energies required to cause failure in the normal, first and second shear directions, respectively.

$G_S = G_s + G_t$, $G_T = G_n + G_S$, and η is a material parameter fit by performing sensitivity analysis.

Denoted by G_n, G_s and G_t are the work done by the tractions and their conjugate relative displacements in the normal, first, and second shear directions, respectively.

b) Adhesive B

Adhesive B is modeled following a bilinear elastic-plastic law. The elastic response is given by:

$$\sigma = E\epsilon \text{ for } \epsilon < \epsilon_y \tag{6}$$

With E The young's modulus and $\epsilon_y = \frac{\sigma_y}{E}$; where σ_y and ϵ_y are the yield stress and strain, respectively.

After yield (σ_y), the stress follows:

$$\sigma = \sigma_y + H(\epsilon_p) \tag{7}$$

Where H is the hardening modulus calibrated from failure stress and strain σ_f and ε_f:

$$H = \frac{\sigma_f - \sigma_y}{\epsilon_f - \epsilon_y} \tag{8}$$

c) *Adhesive C*

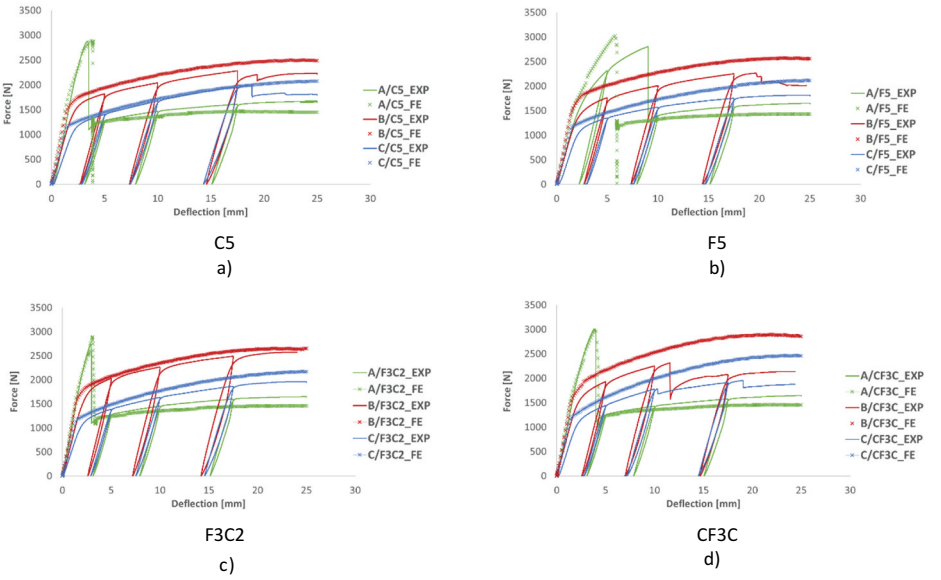
This very flexible adhesive is modeled as a bulk hyperelastic material with a Neo-Hooke strain energy potential:

$$U = C_{10}(I_1 - 3) + \frac{1}{D_1}\left(J^{el} - 1\right)^2 \tag{9}$$

Where I_1 is the first deviatoric strain invariant, C_{10} and D_1 are temperature-dependent material parameters. The latter parameters are required by the Abaqus Standard/implicit solver, and are given by the initial shear modulus μ_0 and bulk modulus K_0 of the adhesive as follows:

$$\mu_0 = 2C_{10}, \quad K_0 = \frac{2}{D_1} \tag{10}$$

Annex C



Comparison of experimental and FE load-deflection curves for specimens bonded to a) C5, b) F5, c) F3C2 and d) CF3C composite patch configuration.